electronics

MDPI

Article

Calibration-Block-Based Tilt-Pose Error Identification and Compensation for Line Confocal Sensors

Yuan Fu [1], Ting Chen [1], Ning Chen [1,*], Bin Guo [1], Yinghui Wang [1], Yinbao Cheng [2] and Chuan Ma [3]

[1] Key Laboratory of Digital Precision Measurement Technology of Zhejiang Province, Zhejiang Institute of Quality Science, Hangzhou 310018, China; fy_9041@163.com (Y.F.); chentingzqs@zuaa.zju.edu.cn (T.C.); urchinbin@163.com (B.G.); 13989835191@163.com (Y.W.)

[2] College of Metrology Measurement and Instrument, China Jiliang University, Hangzhou 310018, China; cyb@cjlu.edu.cn

[3] COSCO SHIPPING Heavy Industry (Zhoushan) Co., Ltd., Zhoushan 316000, China; weng.hailong@coscoshipping.com

* Correspondence: phys2008@163.com

Abstract

Line confocal sensors provide non-contact, high-resolution, and high-efficiency measurement and can be integrated into optical measurement systems such as Photon for three-dimensional topography measurement of complex surfaces. However, installation-induced tilt-pose errors of the sensor can couple height information with lateral position, thereby reducing the accuracy of profile reconstruction. To address this issue, this paper proposes a calibration-block-based tilt-pose error identification and compensation method for line confocal sensors. Using the known geometric features of the calibration block, the proposed method establishes a mapping relationship between sensor tilt-pose errors and measured profile distortion. Sensitivity analysis is performed to identify the dominant error components, and the tilt-pose errors are estimated in a single identification process, enabling quantitative compensation of the measured point cloud. Experimental results show that, after calibration and compensation, the maximum Z-direction height difference in the overlapping profile region of the calibration block is reduced from 12.782 μm to 0.307 μm. The proposed method requires no complex external alignment devices and provides an effective approach for high-precision integrated applications of line confocal sensors.

Keywords: line confocal sensor; surface topography measurement; tilt-pose error calibration; error compensation

Check for updates

Academic Editor: Janos Botzheim

Received: 22 May 2026
Revised: 15 June 2026
Accepted: 17 June 2026
Published: 18 June 2026

Copyright: © 2026 by the authors. Licensee MDPI, Basel, Switzerland. This article is an open access article distributed under the terms and conditions of the Creative Commons Attribution (CC BY) license.

1. Introduction

With the rapid development of semiconductor packaging, new energy batteries, and functional surface manufacturing, microstructures such as solder balls/bumps, bonding wires, microgrooves, electrode coatings, and precision curved surfaces have been widely used in device manufacturing and performance regulation [1–3]. These structures are typically characterized by small feature sizes, subtle local topographical variations, and complex material reflectance characteristics, and the accuracy of their surface topography directly affects device performance. Therefore, high-precision, non-contact, and rapid three-dimensional (3D) detection technologies for complex microstructure surfaces have become essential in advanced manufacturing quality control.

Line confocal measurement acquires surface profile information through line scanning and offers the advantages of non-contact operation, high resolution, and high efficiency.

It has therefore been widely applied to precision measurements of various surface features. The Photon optical measurement system developed by LMI Technologies uses a line confocal sensor to measure surface morphology with submicron axial measurement resolution and can achieve high-speed and high-precision 3D detection of various surface types, including mirror, transparent, semi-transparent, curved, concave–convex, and soft surfaces [4]. LMI technical documentation indicates that the sensor itself is factory calibrated. However, in practical measurement processes, the installation pose error of the line confocal sensor is also an important factor affecting measurement accuracy. In particular, sensor tilt-pose errors cause the measurement optical axis to deviate from its ideal direction, coupling the height information of the measured surface with lateral position and thereby introducing systematic measurement errors [5]. This error may further lead to profile distortion and feature-dimension evaluation errors, especially at step edges, microgrooves, inclined surfaces, curved surfaces, and local height discontinuities.

For the calibration and compensation of tilt-pose errors in optical sensors integrated into measurement systems, existing methods typically use planes, spheres, cylinders, ball bars, or other geometric standards to calibrate the external parameters between the sensor coordinate system and the motion coordinate system [6–8]. Che and Ni [9] proposed a ball-target-based method for the extrinsic calibration of a 3D, multiple-axis, structured-light (laser-stripe) scanning system, reducing the ball-radius-based shape distortion from 1.44 mm to 0.04 mm over an 18.93 mm range. Santolaria et al. [10] developed a one-step calibration method for a laser-triangulation sensor integrated into a joint-arm coordinate measurement system, enabling simultaneous estimation of the laser plane, CCD sensor, and camera, as well as the extrinsic relationship between the sensor and the joint-arm coordinate system. Wang et al. [11] further proposed a pose calibration method for a line-structured light probe in a cylindrical coordinate measurement system based on a standard ball-bar target, reducing the deviations in the fitted sphere centers and radii to within 0.009 mm after probe installation error compensation. In addition to ball-target and ball-bar methods, cylindrical-target and planar-target calibration methods have also been widely investigated. Liu et al. [12] proposed an on-site calibration method using a movable parallel-cylinder target and achieved a calibration accuracy of 0.07 mm over a measurement distance of 700 mm. Sun et al. [13] used a free-placed single cylindrical target for line-structured-light vision sensor calibration, improving the flexibility of target placement and achieving a measurement accuracy of 0.056 mm at a measuring distance of 400 mm. Gao et al. [14] proposed a spatial-geometry-based light-plane calibration method, reducing the RMS error to 0.011 mm, compared with 0.031 mm and 0.075 mm obtained by two reference methods. Zhang et al. [15] developed a simple planar-target-based calibration method for a line-structured light vision system using two placements of a planar target, achieving RMS errors of 0.035 mm for length measurement and 0.054 mm for height measurement.

These studies quantitatively demonstrate that geometric-standard-based calibration methods can effectively improve the calibration and measurement accuracy of optical line sensors [16,17]. However, most existing studies are mainly intended for line-structured light, laser-stripe, or laser-triangulation sensors, and their calibration objectives are generally the light plane, camera parameters, or the extrinsic transformation between the sensor and the motion system. These methods usually rely on standard artifacts such as spheres, ball bars, planes, spherical surfaces, or cylindrical surfaces, whose geometric constraints mainly serve light-plane calibration or coordinate-transformation estimation. For line confocal sensors, surface topography is reconstructed through line scanning and multi-profile stitching. Standard artifacts such as spheres and ball bars have surface normals that vary continuously with position, making it difficult to simultaneously constrain the three-axis tilt-pose errors of a line confocal sensor. Moreover, their error observations are

difficult to directly associate with distortion features in stitched profiles, such as height differences, slope displacement, and in-plane misalignment. Therefore, these methods are difficult to apply directly to the identification and compensation of installation-induced tilt-pose errors in line confocal sensors. In addition, existing studies online confocal sensors have mainly focused on wavelength–height calibration, spectral peak extraction, axial response calibration, and the influence of surface tilt on the confocal response [18,19]. In contrast, relatively few studies have addressed the installation-induced tilt-pose errors that occur after line confocal sensors are integrated into measurement systems, especially the quantitative relationship between three-axis tilt-pose errors and stitched profile deviations.

To address the above issues, this paper proposes a calibration-block-based tilt-pose error identification and compensation method for line confocal sensors. A calibration block with a "plane–slope–plane" feature structure is used to provide multiple explicit geometric constraints for the simultaneous identification of three-axis tilt-pose errors. By establishing a quantitative mapping relationship between sensor tilt-pose errors and stitched profile distortion, the method reveals the mechanism by which the dominant sensitive error components affect profile distortion. The tilt-pose errors are then obtained through a single identification process, enabling direct quantitative compensation of the measured point cloud. This method can effectively reduce systematic measurement errors introduced by sensor installation pose deviations, thereby enabling high-precision surface topography measurement of complex microstructures. The proposed method requires no complex external alignment devices and provides an effective approach for high-precision integrated applications of line confocal sensors.

2. Materials and Methods

2.1. Measurement Principle

The principle of the calibration-block-based tilt-pose error identification and compensation method for line confocal sensors is shown in Figure 1. The Photon optical measurement system mainly consists of a line confocal sensor, an X/Y motion stage, a Z-axis guide rail, a marble pedestal, and a data acquisition module. During measurement, the calibration block or test sample is fixed on the X/Y motion stage, while the line confocal sensor is mounted on the Z-axis guide rail. The relative height between the sensor and the measured surface is adjusted through the Z-axis guide rail so that the height variation in the measured surface falls within the effective measurement range of the sensor.

The line confocal sensor adopts the spectral confocal measurement principle. After a broadband light source passes through a chromatic dispersion objective, light beams of different wavelengths are focused at different axial positions. When the measured surface is located at a specific axial position, only the corresponding wavelength satisfies the optimal focusing condition on the surface and is reflected back to the spectral imager. By extracting the peak wavelength of the returned spectral signal and using the internally established wavelength–height calibration relationship, multiple height values along a single profile line of the measured surface can be obtained. The X/Y motion stage then drives the sample to scan in the X- and Y-directions, and the continuously acquired line-profile data are stitched to reconstruct the 3D profile of the measured surface.

The global coordinate system O-XYZ and the sensor measurement coordinate system O_S-$X_SY_SZ_S$ are established. Suppose that the line confocal sensor measures the i-th profile

sampling point at the j-th scanning position. The theoretical spatial coordinates of the measurement point P_{ij}^0 can be expressed as

$$P_{ij}^0 = \begin{bmatrix} x_{ij}^0 \\ y_{ij}^0 \\ z_{ij}^0 \end{bmatrix} = \begin{bmatrix} x_i + x_{\text{stage}} \\ y_j + y_{\text{stage}} \\ z_{s,ij} + z_{\text{stage}} \end{bmatrix}. \tag{1}$$

where x_i is the sampling position along a single profile acquired by the line confocal sensor, y_j is the position of the motion stage along scanning direction, x_{stage}, y_{stage} and z_{stage} are the positions of the three motion axes of the measurement system, respectively, and $z_{s,ij}$ is the height value of the measured surface obtained by the line confocal sensor.

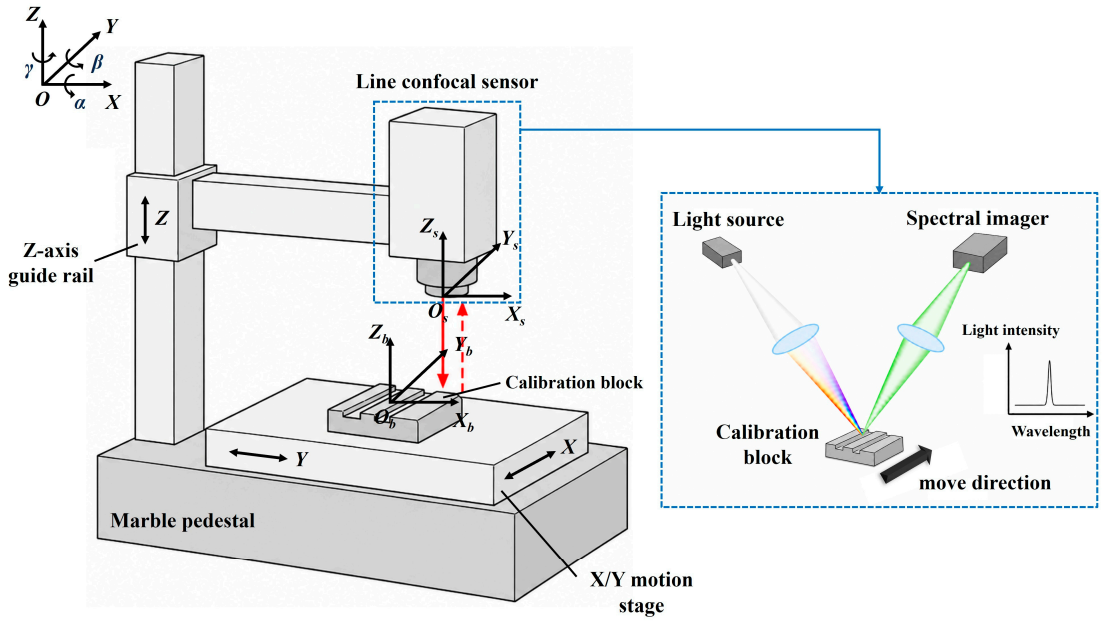


Figure 1. Principle of three-dimensional profile measurement of the calibration block.

When the measurement direction of sensor is inconsistent with that of the measurement system, the measured height is coupled with the lateral sampling position, resulting in nonphysical profile inclination, local misalignment, and geometric distortion in the measured profile. In this study, the known geometric features of the calibration block are used to establish a tilt-pose error model for the sensor. Through a single identification process, the tilt-pose errors of the sensor around the three axes are obtained, and the 3D topography measurement accuracy of the line confocal sensor in the Photon system is improved through error compensation.

2.2. Sensor Tilt-Pose Error Modeling

During practical assembly and alignment, a slight tilt inevitably exists between the sensor measurement coordinate system and the global coordinate system, resulting in deviations between the actual and the theoretical coordinates of the measured points. Let δ_α, δ_β, and δ_γ denote the tilt-pose errors of the line confocal sensor with respect to the global coordinate system around the X-, Y-, and Z-axes, respectively. The actual spatial coordinate of the measured point P_{ij} can then be expressed as

$$P_{ij} = R(\delta_\alpha, \delta_\beta, \delta_\gamma) P_{ij}^0 + T, \tag{2}$$

where $R(\delta_\alpha, \delta_\beta, \delta_\gamma)$ is the rotation matrix corresponding to the sensor tilt-pose errors, and T is the translational installation error of the sensor.

Although the eccentricity of the sensor emission point introduces a translational offset, this offset is mainly constant and can be absorbed by subsequent point-cloud registration. In contrast, angular errors are amplified by the effective lever arm L between the sensor mounting reference and the measurement point. For a small angular error δ, the induced error is approximately $L\delta$, which is usually much larger than the residual influence of a fixed translational offset. Moreover, the angular error varies with position and may cause profile inclination, height mismatch in overlapping regions, and in-plane misalignment. Therefore, this study focuses on rotational tilt-pose errors, which are more critical for stitched profile reconstruction.

The rotation sequence is defined as X–Y–Z. For column vectors, this sequence corresponds to

$$R(\delta_\alpha, \delta_\beta, \delta_\gamma) = R_Z(\delta_\gamma) R_Y(\delta_\beta) R_X(\delta_\alpha), \tag{3}$$

where

$$R_X = \begin{bmatrix} 1 & 0 & 0 \\ 0 & \cos\delta_\alpha & -\sin\delta_\alpha \\ 0 & \sin\delta_\alpha & \cos\delta_\alpha \end{bmatrix}, R_Y = \begin{bmatrix} \cos\delta_\beta & 0 & \sin\delta_\beta \\ 0 & 1 & 0 \\ -\sin\delta_\beta & 0 & \cos\delta_\beta \end{bmatrix}, R_Z = \begin{bmatrix} \cos\delta_\gamma & -\sin\delta_\gamma & 0 \\ \sin\delta_\gamma & \cos\delta_\gamma & 0 \\ 0 & 0 & 1 \end{bmatrix}, \tag{4}$$

For small angular tilt errors in actual installation and adjustment, $\sin\delta \approx \delta$ and $\cos\delta \approx 1$. Therefore, the rotation matrix can be approximated as

$$R(\delta_\alpha, \delta_\beta, \delta_\gamma) = \begin{bmatrix} 1 & -\delta_\gamma & \delta_\beta \\ \delta_\gamma & 1 & -\delta_\alpha \\ -\delta_\beta & \delta_\alpha & 1 \end{bmatrix}, \tag{5}$$

The calibration block consists of multiple known geometric features, with its core measurement region forming a "plane–slope–plane" composite structure. The calibration block is assumed to include a first reference plane S_1, a slope surface S_2, and a second reference plane S_3. Among them, S_1 and S_3 are planar regions with different heights, while S_2 is the sloped region connecting the two planar areas, providing multiple geometric constraints for identifying the sensor tilt-pose errors. Let Ω_k denote the set of measured point-cloud data belonging to the k-th geometric region of the calibration block, where k = 1, 2, 3 correspond to the first reference plane, the slope surface, and the second reference plane, respectively. The mapping relationship between the sensor tilt-pose errors and the measured profile distortion of the calibration block can then be expressed as

$$e_{ij,k}(\delta) = n_k^{\mathrm{T}} R^{-1}(\delta) \left(P_{ij}^0 - T \right) + d_k, (i,j) \in \Omega_k, \tag{6}$$

where $\delta = [\delta_\alpha, \delta_\beta, \delta_\gamma]^{\mathrm{T}}$ is the tilt-pose error parameter vector to be estimated, n_k is the unit normal vector of the k-th theoretical geometric surface, and d_k is the corresponding plane constant.

The residual in Equation (6) represents the point-to-point distance between each measured point and its corresponding theoretical surface. Therefore, minimizing this residual means that the transformed measured point cloud is aligned with the known "plane–slope–plane" geometry of the calibration block. By minimizing the weighted distance residuals between the measured point cloud and the theoretical geometric model, the sensor tilt-pose

errors with respect to the measurement system can be inversely estimated. The objective function can be expressed as

$$\min_{\delta} F(\delta) = \sum_{k=1}^{3} \sum_{(i,j\in\Omega_k)} W_k \left[e_{ij,k}(\delta) \right]^2, \tag{7}$$

where W_k is the weight coefficient of the k-th geometric region and can be determined from the plane-fitting standard deviation σ_k of that region, and ε is a small constant used to avoid division by zero.

$$W_k = \frac{1}{\sigma_k^2 + \varepsilon}, \tag{8}$$

The weight coefficient is introduced to account for the different fitting uncertainties of the three regions. Regions with smaller fitting standard deviations are assigned larger weights, whereas regions affected by noise or edge-transition effects are assigned smaller weights. The standard deviation σ_k is calculated from the point-to-point fitting residuals of the k-th geometric region as

$$\sigma_k = \sqrt{\frac{1}{N_k - 1} \sum_{i,j\in\Omega_k} \left(e_{ij,k} \right)^2}. \tag{9}$$

where N_k is the number of measurement points in region S_k.

2.3. Sensitivity Analysis

During sensor mounting, small angular deviations are difficult to completely avoid, and their magnitude is usually on the order of 0.1°. Therefore, the representative angular error of 0.2° is selected according to preliminary alignment observations of the integrated measurement system to illustrate the distortion mechanism caused by each angular component. To clarify the influence of tilt-pose errors on the measurement results, the Y-Z sectional profile distortions of the calibration block are simulated for three representative orientations, namely 0°, 45°, and 90°. Based on the established sensor tilt-pose error model, the tilt-pose errors δ_α, δ_β, and δ_γ are individually set to 0.2°, and the distorted stitched profile is compared with the ideal profile. The black dashed line represents the theoretical Y-Z sectional profile of the calibration block at the corresponding orientation, which should exhibit a "plane–slope–plane" structure. The blue solid line represents the nonphysical distorted profile caused by the tilt-pose error.

As shown in Figure 2a, δ_α mainly induces nonphysical height variation along the scanning Y-direction, and its influence is weakly dependent on the orientation of the calibration block. Whether the calibration block is placed at 0°, 45°, or 90°, the distorted profile exhibits an evident height inclination or height offset relative to the theoretical profile. As shown in Figure 2b, δ_β mainly causes a height deviation in the Z-direction. When the calibration block is placed at 0° and 45°, the distorted profile mainly shows an overall height elevation and a shift in the slope position relative to the theoretical profile. As shown in Figure 2c, δ_γ does not directly introduce a significant Z-direction height error in the Y-Z section. Instead, it mainly causes lateral misalignment in the X-Y plane, thereby affecting the reconstruction of geometric features such as slopes, edges, and grooves. When the calibration block is rotated to 90°, the relative relationship between the fixed Y-Z section and the edge or slope direction of the calibration block changes. As a result, slight local misalignment or a small step can be observed.

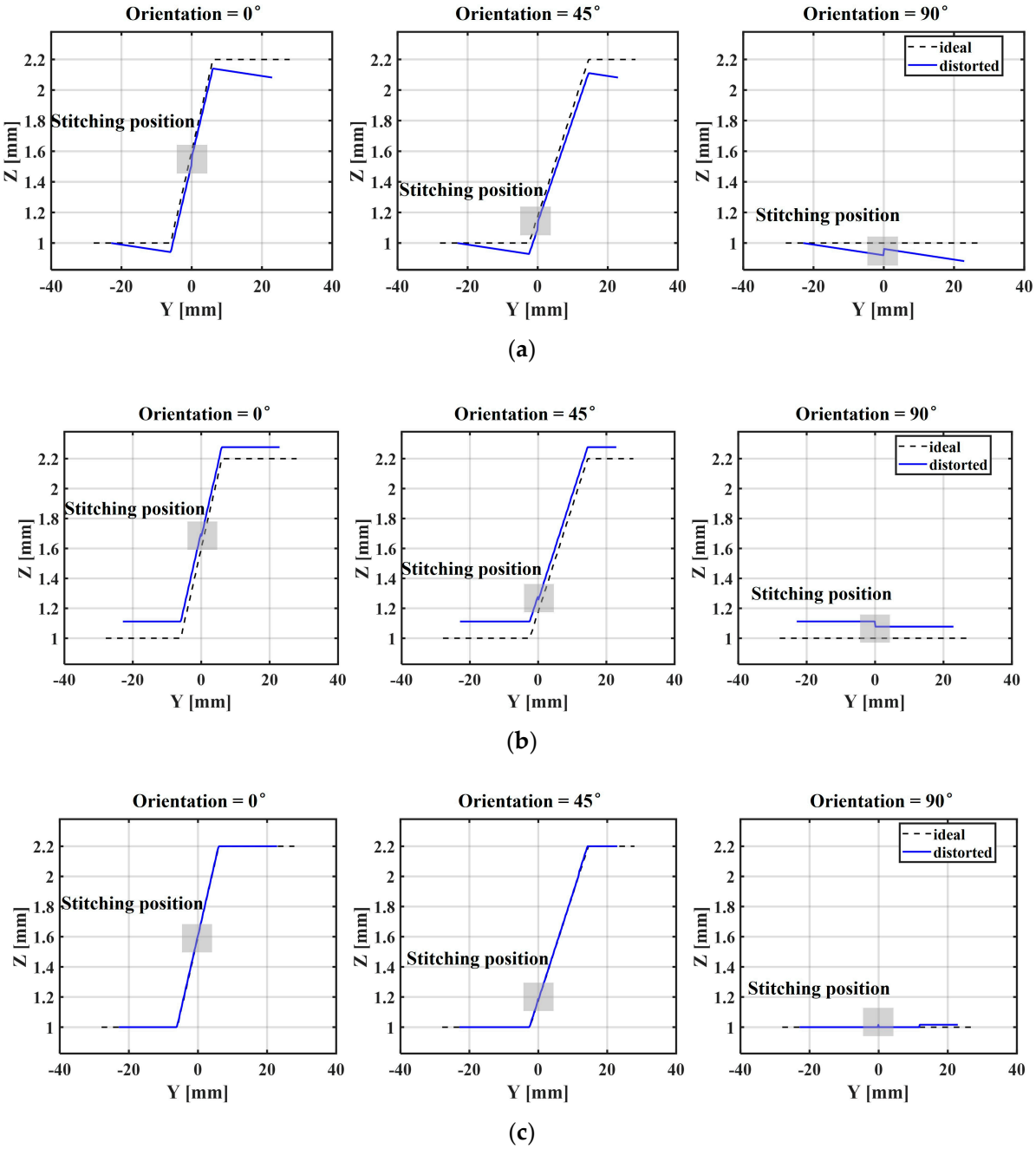
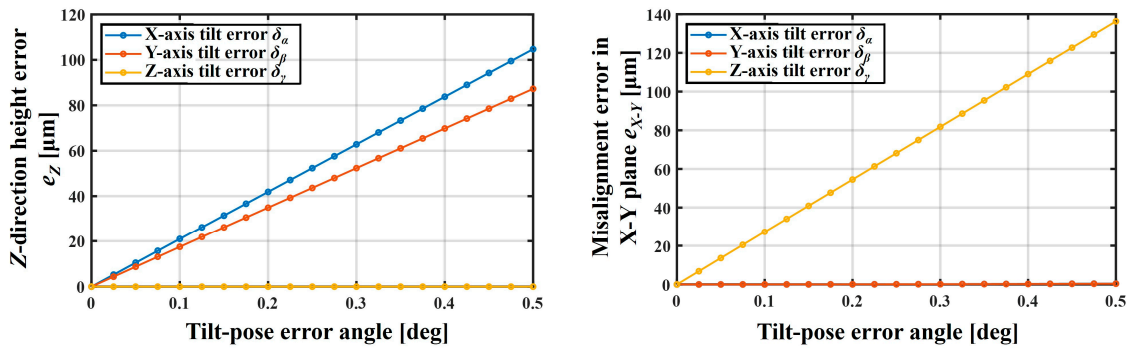


Figure 2. Y-Z sectional profile distortions in the stitched measurement data of the calibration block placed at orientations of 0°, 45°, and 90° under a tilt error of 0.2° around each axis. (**a**) Profile distortion caused by the tilt-pose error $\delta_\alpha = 0.2°$. (**b**) Profile distortion caused by the tilt-pose error $\delta_\beta = 0.2°$. (**c**) Profile distortion caused by the tilt-pose error $\delta_\gamma = 0.2°$.

Sensitivity analysis of various tilt-pose errors is conducted with respect to the height error in the overlapping profile region and the misalignment error in the X-Y plane. Based on the established sensor tilt-pose error model, the angular error range of 0–0.5° is selected as a conservative small-angle, assembly-error interval for sensitivity evaluation. This range is used to cover possible installation deviations under practical assembly conditions and to compare the relative influence of different angular error components on the reconstructed profile. The profile measurement errors introduced by each individual error component are simulated, as shown in Figure 3.



(**a**) (**b**)

Figure 3. Simulation of the influence of tilt-pose errors varying within [0°, 0.5°] on profile measurement results. (**a**) Height error in the overlapping profile region. (**b**) Misalignment error in the X-Y plane.

Figure 3a shows the influence of different tilt-pose errors on the Z-direction height error. The simulation results indicate that the tilt-pose errors around the X-axis, δ_α, and the Y-axis, δ_β, both cause significant Z-direction height errors, and the induced error increases approximately linearly with the tilt angle. In contrast, the tilt-pose error around the Z-axis, δ_γ, has little influence on the Z-direction height error and can almost be neglected. Therefore, for height reconstruction, δ_α and δ_β are the dominant sensitive error components. Figure 3b shows the influence of different tilt-pose errors on the misalignment error in the X-Y plane. It can be seen that the tilt-pose error around the Z-axis, δ_γ, causes obvious in-plane misalignment in the X-Y plane, and the misalignment error increases approximately linearly with the tilt angle. This may affect the stitching and positioning of geometric features such as slopes, edges, and grooves. In contrast, δ_α and δ_β have only a minor influence on the misalignment error in the X-Y plane.

Therefore, for profile reconstruction aimed at surface height, δ_α and δ_β are the sensitive error components. For measured surfaces containing geometric features such as slopes, edges, and grooves, although δ_γ does not directly introduce first-order height errors, it affects the in-plane registration relationship between the measured point cloud and the theoretical model. Therefore, it still needs to be jointly estimated.

The three point-cloud regions S_1, S_2, and S_3 are selected according to the known "plane–slope–plane" structure of the calibration block, and points near edge-transition boundaries are excluded before fitting. The nonlinear least-squares method is then used to jointly estimate the tilt-pose errors of the sensor in three directions. The initial value of the tilt-pose error vector is set as $\delta^{(0)} = [0, 0, 0]^{\mathrm{T}}$. Let $e^{(r)}$ and $J^{(r)}$ denote the residual vector and the Jacobian matrix obtained after the r-th iteration, respectively. The parameter increment can be expressed as

$$\Delta\delta^{(r)} = -\left[\left(J^{(r)}\right)^T W J^{(r)} + \lambda I\right]^{-1} \left(J^{(r)}\right)^T W e^{(r)}, \tag{10}$$

The tilt-pose error parameters are then updated iteratively as

$$\delta^{(r+1)} = \delta^{(r)} + \Delta\delta^{(r)}, \tag{11}$$

The iteration is terminated when the increment in the error parameters is smaller than the angular convergence threshold ε_δ.

$$\left\|\Delta\delta^{(r)}\right\|_2 \leq \varepsilon_\delta. \tag{12}$$

The nonlinear least-squares iteration is terminated when the termination condition is satisfied, or when the maximum number of iterations $N_{\max}$ is reached. In this study, ε_δ is set to 10^{-11}, and $N_{\max}$ is set to 1000. After the termination condition is satisfied, the optimal estimates of sensor tilt-pose errors in three directions can be obtained. These estimated parameters are then incorporated into the established error model to achieve calibration and compensation of the sensor tilt-pose errors.

3. Results

3.1. Measurement System

As shown in Figure 4, a Photon optical measurement system developed by LMI was used to perform 3D scanning measurements of both the test workpiece and the calibration block according to the proposed method.

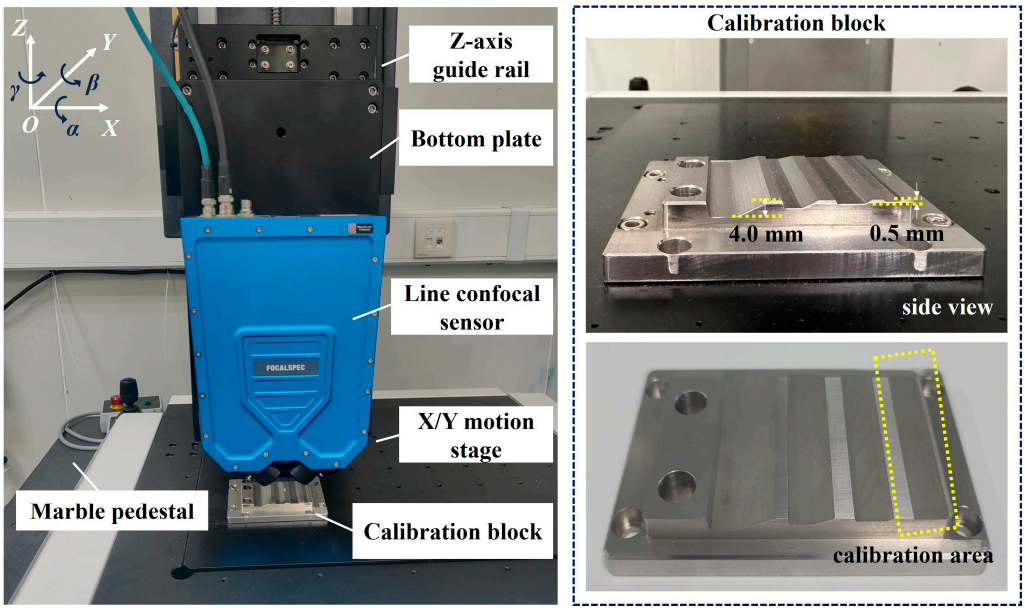


Figure 4. LMI Photon optical measurement system and the calibration block.

The measurement system is equipped with an LCI 401 line spectral confocal sensor, with a measurement range of 8.0 mm and a depth of field of 1.1 mm, enabling submicron scanning accuracy. The calibration block contains four calibration regions, each consisting of a "plane–slope–plane" structure. The height differences between the two planes in these four regions are 4.0 mm, 2.0 mm, 1.0 mm, and 0.5 mm, respectively. Due to the limited depth of field of the sensor, the fourth region is selected as the calibration region in this study. For the proposed tilt-pose error identification method, the key metrological parameter of the calibration block is the height difference between the two reference planes, because this value directly defines the reference geometry used in the plane–slope–plane constraint. The height difference in the calibration block was calibrated by the National Institute of Metrology, China. The main parameters of the calibration block are shown in Table 1. The experimental conditions were a temperature of 23.0 ± 2.0 °C and a humidity of 51% ± 10% RH.

Table 1. Main parameters of the calibration block.

Material	Number of Calibration Regions	Nominal Height Differences	Height Differences Measurement Uncertainty (k = 2)	Flatness of the Reference Planes	Surface Roughness
Stainless steel	4	4.0 mm, 2.0 mm, 1.0 mm, 0.5 mm	0.1 μm	1 μm	Ra 0.5 μm

3.2. Sensor Tilt-Pose Error Calibration and Compensation Experiment

The calibration block was used as the test workpiece and fixed on the worktable. Based on the bottom plane of the calibration area, the Z-axis was driven until the bottom plane was located within the measurement range of the sensor. The Y-axis was then driven, and the sensor was used to perform line scanning of the surface features in the calibration region of the calibration block. The complete surface topography was obtained by stitching the acquired line profiles.

The measured surface topography of the calibration block before sensor tilt-pose error calibration is shown in Figure 5a. Due to the sensor tilt-pose errors, obvious distortion can be observed in the stitched surface profile of the calibration block. The measured surface topography after sensor tilt-pose error calibration is shown in Figure 5b. The angular errors around X-, Y-, and Z-axes were solved using the proposed error model as $\delta_\alpha = +0.2033^\circ$, $\delta_\beta = +0.0111^\circ$, and $\delta_\gamma = -0.2410^\circ$, respectively. As shown in Figure 5c, before calibration, obvious height inconsistency can be observed between adjacent stitched profiles in the overlapping regions. The maximum Z-direction height difference between the two profiles in the overlapping area after profile stitching was 12.782 μm. After the identified tilt-pose error values were incorporated into the model, the height mismatch in the overlapping regions was significantly reduced, as shown in Figure 5d. The maximum Z-direction height difference in the overlapping area was reduced to only 0.307 μm. The dashed lines indicate the overlapping regions between adjacent profile pairs. This result demonstrates that the proposed method can effectively suppress profile distortion caused by sensor installation tilt-pose errors.

To evaluate the repeatability of the proposed calibration procedure, the calibration block was removed and repositioned on the worktable before each calibration trial. The sensor and motion system were kept fixed during the repeated tests. A total of five independent calibration trials were conducted. In each trial, the selected calibration region was scanned, the tilt-pose error parameters δ_α, δ_β, and δ_γ were identified, and the measured point cloud was compensated using the identified parameters. The maximum Z-direction height difference in the overlapping profile region after compensation was used as the indicator of compensation accuracy. The results of repeated calibrations are shown in Table 2.

Table 2. Repeated calibration results of tilt-pose errors.

No.	δ_α (Deg)	δ_β (Deg)	δ_γ (Deg)	Max. ΔZ After Compensation (μm)
1	+0.2052	+0.0188	−0.2425	0.288
2	+0.2036	+0.0102	−0.2438	0.295
3	+0.2032	+0.0185	−0.2411	0.292
4	+0.2044	+0.0155	−0.2394	0.302
5	+0.2018	+0.0128	−0.2405	0.310
Mean δ_α (deg)		+0.2036	δ_α measurement repeatability (deg)	0.0013
Mean δ_β (deg)		+0.0152	δ_β measurement repeatability (deg)	0.0037
Mean δ_γ (deg)		−0.2415	δ_γ measurement repeatability (deg)	0.0017

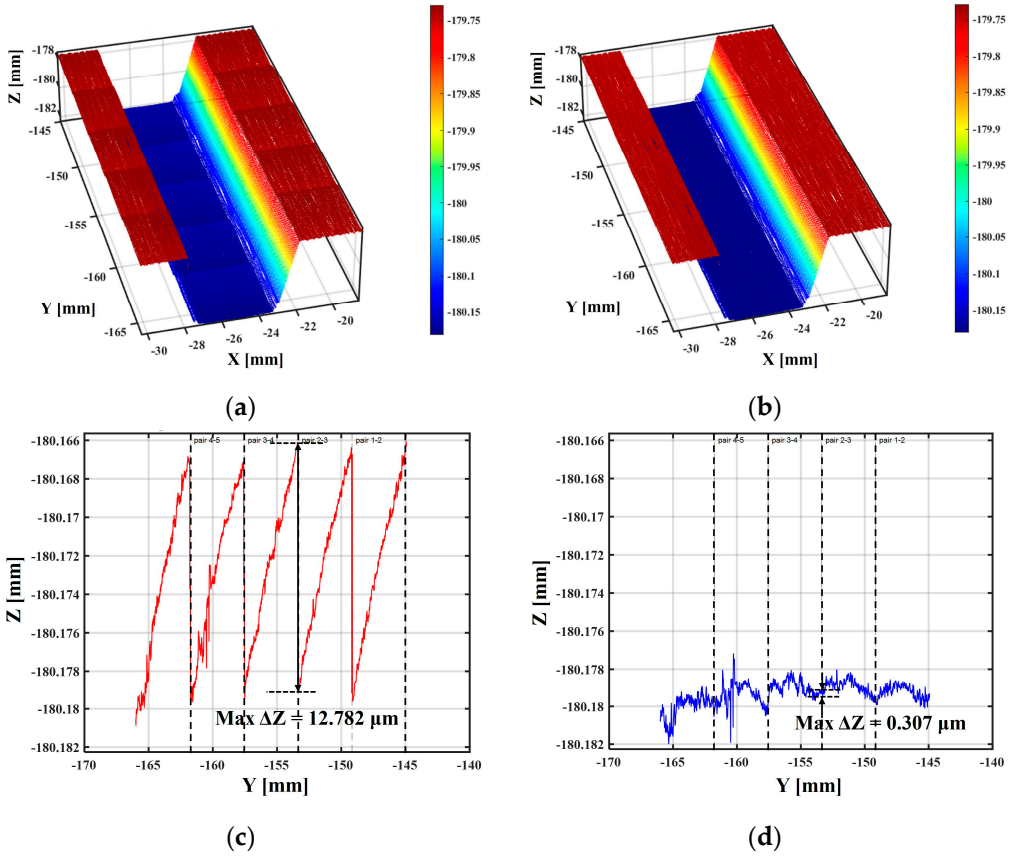


Figure 5. Three-dimensional topography measurement results of the calibration area of the calibration block. (**a**) Measurement result before calibration. (**b**) Measurement result after calibration. (**c**) Height difference in the overlapping profile area before calibration. (**d**) Height difference in the overlapping profile area after calibration.

The results show that the identified angles have good repeatability, and the compensated maximum height difference remains at the sub-micrometer level.

3.3. Three-Dimensional Topography Measurement Experiment

3.3.1. Three-Dimensional Topography Measurement of the Standard Step Sample

To verify the feasibility of the proposed method, a standard step sample with a period of 100 μm was used as the test workpiece and fixed on the worktable for 3D surface topography measurement. The Z-axis was driven until the surface to be measured was located within the measurement range of the sensor. The Y-axis was then driven, and the sensor was used to perform line scanning of the measured surface, after which the complete topography was obtained by stitching the acquired profiles.

The measured topography of the step sample before error compensation is shown in Figure 6a. After the identified sensor tilt-pose errors were compensated in the measured point-cloud data, the corrected 3D topography was obtained, as shown in Figure 6b. To further show the microstructural features of the measured sample, the central region of the compensated topography is locally enlarged, as shown in Figure 6c. The enlarged view clearly reveals the periodic grating structure of the measured sample. The two-dimensional profile extracted at the center is shown in Figure 6d. The measurement results indicate that, before error compensation, the measured period of the standard step sample was 120.2 μm, and obvious profile discontinuities can be observed at the stitching positions. The red dashed line indicates the data stitching seam between two adjacent scan regions. After calibration and compensation of the sensor tilt-pose errors, the profile distortion of

the measured topography was significantly suppressed, and the measured step period decreased to 102.0 μm, which is closer to the nominal period of 100 μm.

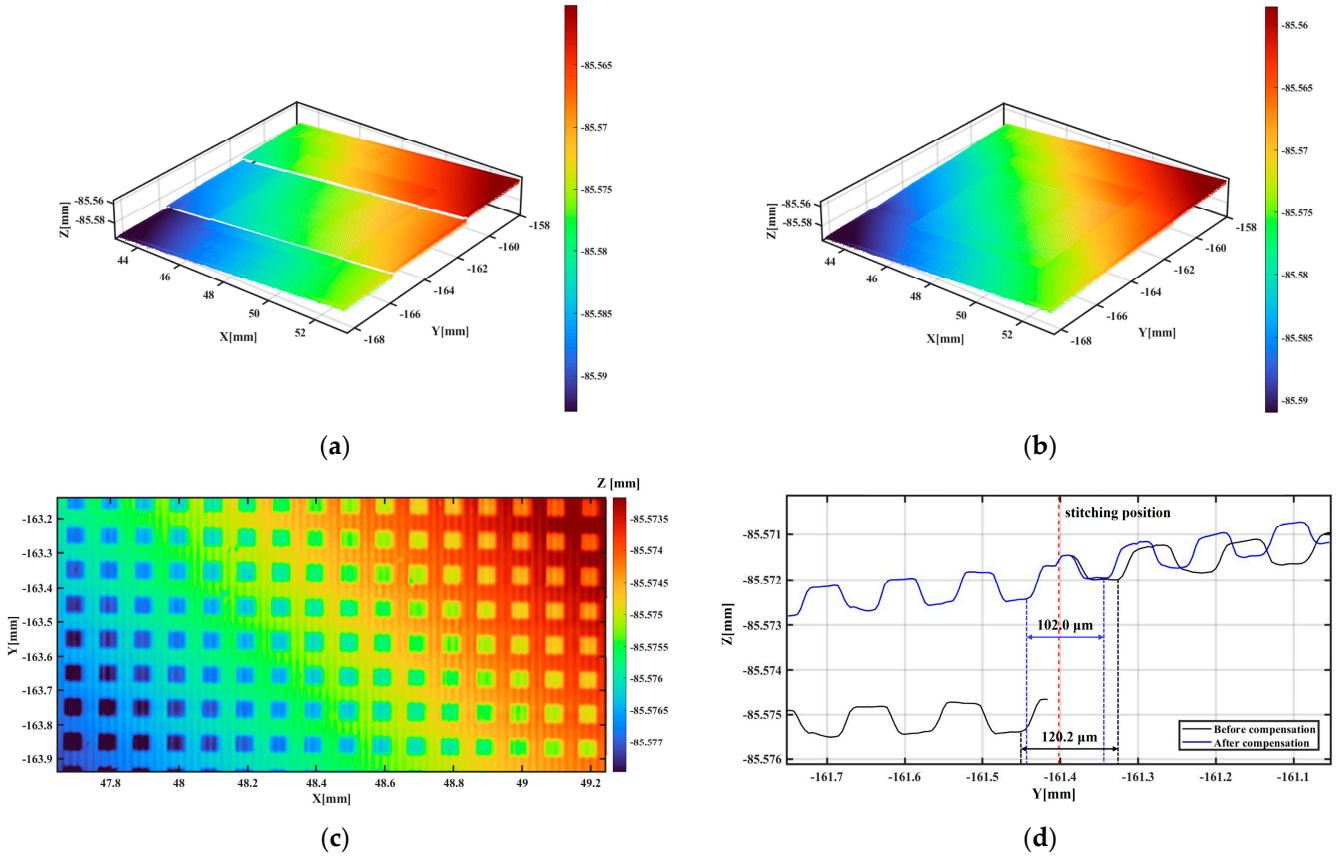


Figure 6. Three-dimensional topography measurement results of the standard step sample. (**a**) Topography measurement result before error compensation. (**b**) Topography measurement result after error compensation. (**c**) Enlarged view of the compensated topography. (**d**) Two-dimensional profile extracted from the center of the measured sample before and after error compensation.

To verify the stability of the proposed method, ten repeated measurements were performed on the standard step sample. The period measurement results of the standard step sample before and after error compensation are listed in Table 3. After error compensation, the mean measured period of the standard step sample was 102.2 μm, and the period measurement repeatability was 0.5 μm (3σ).

Table 3. Period measurement results of the standard step sample before and after compensation.

No.	Period Before Compensation (μm)	Period After Compensation (μm)	No.	Period Before Compensation (μm)	Period After Compensation (μm)
1	120.3	102.1	6	120.5	102.5
2	120.2	102.0	7	120.2	102.2
3	120.5	102.2	8	120.4	102.1
4	120.2	102.3	9	120.3	102.1
5	120.2	102.2	10	120.6	102.5
Mean measured period after compensation (μm)		102.2	Period measurement repeatability (3σ) (μm)		0.5

The experimental results demonstrate that the proposed method can effectively identify the installation tilt-pose errors of the line confocal sensor with respect to the mea-

surement system and significantly reduce the profile distortion and height measurement deviations caused by these errors. Consequently, the accuracy and stability of the line confocal sensor in surface topography measurement of complex microstructures are improved.

3.3.2. Three-Dimensional Topography Measurement of the Standard Thickness Sample

To further verify the measurement accuracy of the proposed method, a 3D topography measurement experiment was performed using a standard thickness sample. The standard thickness sample was calibrated by the National Institute of Metrology, China, and its standard depth value is 1.982 μm. During the experiment, the standard thickness sample was fixed on the worktable, and the Z-axis position was adjusted to ensure that the sample surface was within the measurement range of the line confocal sensor. Subsequently, the Y-axis was driven to move, and the line confocal sensor was used to acquire the surface profile data of the sample. The 3D point cloud of the standard thickness sample was obtained by stitching multiple profiles, and the identified sensor tilt-pose errors were then compensated in the measured point-cloud data.

The two-dimensional height measurement result of the standard thickness sample surface morphology after error compensation is shown in Figure 7a. The measurement result indicates that the local micrometer-scale depth features of the standard thickness sample can be clearly distinguished. To extract the true depth feature of the sample, a Y-Z two-dimensional profile was extracted at the central section, as shown in Figure 7b. Tilt removal was then performed on the extracted two-dimensional profile, as shown in Figure 7c. The average depth of the test sample was calculated to be 2.133 μm. Compared with the standard average depth value provided by the National Institute of Metrology, China, the measurement deviation was 0.151 μm.

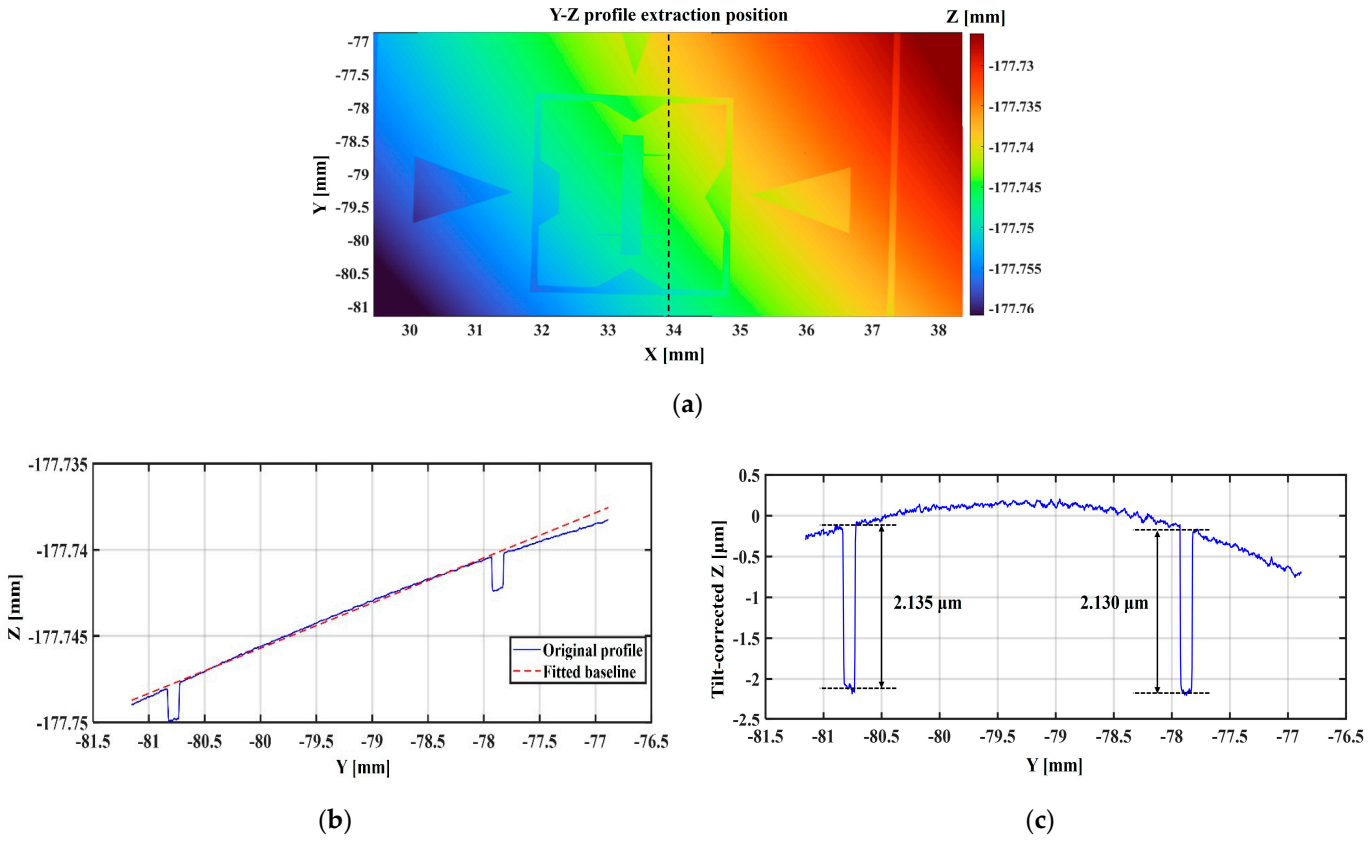


Figure 7. Three-dimensional topography measurement results of the standard thickness sample. (**a**) Two-dimensional height measurement result after error compensation. (**b**) Y-Z two-dimensional profile extracted at the central section. (**c**) Tilt-corrected two-dimensional profile.

The experimental results show that the proposed method can achieve high-precision 3D topography measurement of a micrometer-scale standard thickness sample, further verifying its applicability to samples with different microstructural features.

3.4. Uncertainty Analysis

To evaluate the measurement reliability of the proposed method, the uncertainty of the compensated measurement result is analyzed based on the repeated period measurements of the standard step sample. The standard uncertainty components mainly include repeated measurement error, system measurement error, and calibration-block geometric error. These factors jointly affect the dimensional measurement results.

3.4.1. Repeated Measurement Error

The standard uncertainty component u_1 introduced by repeated measurement of the standard step sample is evaluated from 10 repeated measurements, and the experimental standard deviation is calculated as s = 0.167 μm. Therefore, the standard uncertainty introduced by repeated measurements is

$$u_1 = \frac{0.167}{\sqrt{10}} = 0.053 \text{ μm}, \tag{13}$$

3.4.2. System Measurement Error

The standard uncertainty component u_2 introduced by the measurement error of the Photon optical measurement system is evaluated according to the Z-direction repeatability. The Z-direction repeatability of the Photon system is 0.05 μm. Therefore, the standard uncertainty introduced by the system measurement error is

$$u_2 = \frac{0.05}{\sqrt{3}} = 0.029 \text{ μm}, \tag{14}$$

3.4.3. Calibration-Block Geometric Error

The standard uncertainty component u_3 introduced by the height error of the calibration block is evaluated according to the calibrated height difference in the selected calibration region. The height measurement error of the calibration block is 0.05 μm. Therefore, the standard uncertainty introduced by the calibration block height error is

$$u_3 = 0.05 \text{ μm}. \tag{15}$$

Combining these uncertainties yields u_{cr} as

$$u_{cr} = \sqrt{u_1^2 + u_2^2 + u_3^2} = \sqrt{0.053^2 + 0.029^2 + 0.05^2} = 0.078 \text{ μm}, \tag{16}$$

With a coverage factor of k = 2, the expanded uncertainty is

$$U = k \times u_{cr} = 0.156 \text{ μm}. \tag{17}$$

Therefore, the compensated period measurement result of the standard step sample can be expressed as $p = 102.2 \pm 0.156$ μm (k = 2).

4. Discussion

A novel calibration-block-based method for tilt-pose error identification and compensation of line confocal sensors is proposed in this study. By using the known geometric features of the calibration block, the proposed method establishes a mapping relationship

between sensor tilt-pose errors and the measured profile distortion of the calibration block. Sensitivity analysis of angular errors in different directions is performed to determine the dominant error components, which are then calibrated and quantitatively compensated. The proposed method can effectively reduce systematic measurement errors introduced by sensor installation pose deviations. Experimental results show that, after calibration and compensation, the maximum *Z*-direction height difference in the overlapping profile area of the calibration block is reduced from 12.782 μm to 0.307 μm. A 3D topography measurement experiment is also conducted on a standard step sample. After error compensation, the measured topography exhibited no obvious distortion, and the measured period is 102.0 μm. Furthermore, ten repeated measurements are performed on the standard step sample. The mean measured period after compensation is 102.2 μm, and the period measurement repeatability is 0.5 μm (3σ). Based on the uncertainty analysis, the compensated period measurement result can be expressed as $p = 102.2 \pm 0.156$ μm ($k = 2$), indicating good repeatability of the proposed method.

In summary, the proposed method enables one-step calibration and compensation of line confocal sensor tilt-pose errors without relying on external alignment device, providing an effective approach for high-precision integrated applications of line confocal sensors.

Author Contributions: Conceptualization, Y.F. and T.C.; methodology, Y.F.; software, Y.F.; validation, Y.F. and N.C.; formal analysis, Y.F.; investigation, B.G.; resources, Y.W.; data curation, Y.F.; writing—original draft preparation, Y.F.; writing—review and editing, N.C.; visualization, Y.C.; supervision, C.M.; project administration, N.C.; funding acquisition, N.C. All authors have read and agreed to the published version of the manuscript.

Funding: This research was funded by the Science and Technology Plan Project of Zhejiang Administration for Market Regulation, grant number ZD2025008.

Data Availability Statement: The research data presented in this work are available upon request.

Conflicts of Interest: Author Chuan Ma was employed by the company COSCO SHIPPING Heavy Industry (Zhoushan) Co., Ltd. The remaining authors declare that the research was conducted in the absence of any commercial or financial relationships that could be construed as a potential conflict of interest.

References

1. Bender, E.; Bernstein, J.B.; Boning, D.S. Modern Trends in Microelectronics Packaging Reliability Testing. *Micromachines* **2024**, *15*, 398. [CrossRef] [PubMed]
2. Reynolds, C.D.; Slater, P.R.; Hare, S.D.; Simmons, M.J.H.; Kendrick, E. A Review of Metrology in Lithium-Ion Electrode Coating Processes. *Mater. Des.* **2021**, *209*, 109971. [CrossRef]
3. Xu, X.; Cheng, L.; Zhao, X.; Wang, J.; Chen, X. Micro/Nano Periodic Surface Structures and Performance of Stainless Steel Machined Using Femtosecond Lasers. *Micromachines* **2022**, *13*, 976. [CrossRef] [PubMed]
4. LMI Technologies. *PHOTON™ Optical Inspection System Brochure*; LMI Technologies: Burnaby, BC, Canada, 2022.
5. Sato, R.; Shimizu, Y.; Matsukuma, H.; Gao, W. Influence of Surface Tilt Angle on a Chromatic Confocal Probe with a Femtosecond Laser. *Appl. Sci.* **2022**, *12*, 4736. [CrossRef]
6. Wang, S.; Zhao, Q. Development of an On-Machine Measurement System with Chromatic Confocal Probe for Measuring the Profile Error of off-Axis Biconical Free-Form Optics in Ultra-Precision Grinding. *Measurement* **2022**, *202*, 111825. [CrossRef]
7. Xie, Z.; Yu, P.; Gong, H.; Chi, S.; Gao, X. Flexible Scanning Method by Integrating Laser Line Sensors with Articulated Arm Coordinate Measuring Machines. *Chin. J. Mech. Eng.* **2022**, *35*, 116. [CrossRef]
8. Xi, M.; Wang, Y.; Liu, H.; Xiao, H.; Li, X.; Li, H.; Ding, Z.; Jia, Z. Calibration of Beam Vector Deviation for Four-Axis Precision on-Machine Measurement Using Chromatic Confocal Probe. *Measurement* **2022**, *194*, 111011. [CrossRef]
9. Che, C.; Ni, J. A Ball-Target-Based Extrinsic Calibration Technique for High-Accuracy 3-D Metrology Using off-the-Shelf Laser-Stripe Sensors. *Precis. Eng.* **2000**, *24*, 210–219. [CrossRef]
10. Santolaria, J.; Guillomía, D.; Cajal, C.; Albajez, J.A.; Aguilar, J.J. Modelling and Calibration Technique of Laser Triangulation Sensors for Integration in Robot Arms and Articulated Arm Coordinate Measuring Machines. *Sensors* **2009**, *9*, 7374–7396. [CrossRef] [PubMed]

11. Wang, Z.; Zhang, X.; Shen, Y.; Zheng, Z. Pose Calibration of Line Structured Light Probe Based on Ball Bar Target in Cylindrical Coordinate Measuring Machines. *Measurement* **2021**, *171*, 108760. [CrossRef]
12. Liu, Z.; Li, X.; Yin, Y. On-site Calibration of Line-structured Light Vision Sensor in Complex Light Environments. *Opt. Express* **2015**, *23*, 29896–29911. [CrossRef] [PubMed]
13. Sun, J.; Ding, D.; Cheng, X.; Zhou, F.; Zhang, J. Calibration of Line-structured Light Vision Sensor Based on Free-placed Single Cylindrical Target. *Opt. Lasers Eng.* **2022**, *152*, 106951. [CrossRef]
14. Gao, H.; Xu, G.; Ma, Z. A Novel Calibration Method of Line Structured Light Plane Using Spatial Geometry. *Sensors* **2023**, *23*, 5929. [CrossRef] [PubMed]
15. Zhang, Z.; Zhang, H.; Wu, Y.; Zhang, F. Simple and Precise Calibration of the Line-structured Light Vision System Using a Planar Target. *J. Opt. Soc. Am. A* **2023**, *40*, 1397–1408. [CrossRef] [PubMed]
16. Chen, Z.; Wang, Z.; Ren, M.; Zhang, X.; Zhu, L.; Jiang, X. Development of an On-Machine Measurement System for Ultra-Precision Machine Tools Using a Chromatic Confocal Sensor. *Precis. Eng.* **2022**, *74*, 232–241. [CrossRef]
17. Liu, Q.; Yuan, Z.; Di, H.; Sun, S. Global Calibration of an On-Machine Measurement System Using a Chromatic Confocal Sensor. *Precis. Eng.* **2025**, *96*, 864–873. [CrossRef]
18. Qin, M.; Xiong, X.; Xiao, E.; Xia, M.; Gao, Y.; Xie, H.; Luo, H.; Zhao, W. A Kernel-Based Calibration Algorithm for Chromatic Confocal Line Sensors. *Sensors* **2024**, *24*, 6649. [CrossRef] [PubMed]
19. Bai, J.; Li, X.; Wang, X.; Zhou, Q.; Ni, K. Chromatic Confocal Displacement Sensor with Optimized Dispersion Probe and Modified Centroid Peak Extraction Algorithm. *Sensors* **2019**, *19*, 3592. [CrossRef] [PubMed]

Disclaimer/Publisher's Note: The statements, opinions and data contained in all publications are solely those of the individual author(s) and contributor(s) and not of MDPI and/or the editor(s). MDPI and/or the editor(s) disclaim responsibility for any injury to people or property resulting from any ideas, methods, instructions or products referred to in the content.